



Supporting Online Material for

Reactivity of the Gold/Water Interface During Selective Oxidation Catalysis

Bhushan N. Zope, David D. Hibbitts, Matthew Neurock, Robert J. Davis*

*To whom correspondence should be addressed. E-mail: rjd4f@virginia.edu

Published 1 October 2010, *Science* **330**, 74 (2010)

DOI: 10.1126/science.1195055

This PDF file includes:

Materials and Methods
SOM Text
Figs. S1 to S8
Tables S1 to S4
Scheme S1
References

Supporting Online Material

Materials and Methods:

The following commercial catalysts were used in this study: Au/C (World Gold Council, WGC, 0.8 wt%, dispersion 0.05 (*SI*)), Au/TiO₂ (WGC, 1.6 wt%, dispersion 0.29 (*SI*), Pt/C (Sigma-Aldrich, 1 wt%, dispersion 0.43) and Pd/C (Sigma-Aldrich, 3 wt%, dispersion 0.33 (*S2*)) (Table S2) (Dispersion was calculated by H₂ chemisorption for Pt/C and Pd/C and was based on Au particle size for the Au catalysts). Glycerol [Acros, 99.6% purity] or ethanol [Sigma-Aldrich, 99.5%] and NaOH [Mallinckrodt, 99%] were used to prepare the liquid reactant for the reaction. All unlabeled gases used in the study (dioxygen, carbon monoxide, dinitrogen and helium) were of ultra high purity grade [GT&S]. The labeled gases ¹⁸O₂ [$\geq 97\%$ ¹⁸O], C¹⁸O₂ [95% ¹⁸O] and water (H₂¹⁸O) [97% ¹⁸O] were obtained from Cambridge Isotope Laboratories.

Semi-batch oxidation studies were performed in a 50 cm³ Parr Instrument Company 4592 batch autoclave reactor. The aqueous feed solution (30mL, 0.3M glycerol or 0.3M ethanol, 0.6M NaOH) and a proper amount of catalyst were added to the reactor that was then sealed, purged with He and heated to 333 K. The reaction was started by pressurizing the reactor with 150 psig O₂ pressure. For labeled experiments with ¹⁸O₂ gas, the oxidation was carried-out with 50 psig ¹⁸O₂ pressure to minimize waste of the gas. Experiments with labeled water (H₂¹⁸O) used 5mL of reactant solution. The glycerol to Au ratio was determined by calculating the maximum O₂ mass transfer rate (gas → liquid) using the sulfite oxidation method (*SI*). Dioxygen was continually fed in a semi-batch manner to maintain a constant head pressure in the reactor. Samples were periodically removed through the sample diptube and were filtered using a syringe filter (0.2 μm)

before analyzing in a Waters e2695 high pressure liquid chromatograph (HPLC). In case of ethanol oxidation, only one sample was collected at the end of the reaction. The reactor was allowed to cool to room temperature before sampling to avoid loss of volatile substrate. The HPLC was equipped with refractive index detector and UV-VIS detectors. Product separation in the HPLC was carried out using an Aminex HPX-87H column (Bio-Rad) operating at 318 K with 5mM H₂SO₄ as eluent flowing at 0.5 cm³ min⁻¹. The retention times and calibration curves were found using known concentrations of products. A liquid chromatograph equipped with a mass spectrometer (LC-MS, Waters ZQ-MS) was used to identify labeled products formed during the oxidation. When the MS detector was used, 0.01M formic acid was used as eluent in the HPLC.

Product sample from labeled experiments were analyzed in two ways, by direct infusion into the mass spectrometer (MS) and also by first separating the products in the HPLC followed by detection in the mass spectrometer. Acid products analyzed through the Aminex column in the HPLC showed significant oxygen exchange resulting in a change in the isotope distribution. For example, Figures S7C and S7D show the acetic acid spectra from ethanol oxidation experiment over Au/TiO₂ with H₂¹⁸O analyzed through the liquid chromatograph (HPLC) followed by MS detection and analyzed by direct infusion in MS, respectively. No ¹⁸O was observed in the acetic acid product when it was analyzed using the HPLC column, whereas two ¹⁸O atoms were observed when the product was infused directly in the mass spectrometer, indicating that considerable exchange of oxygen occurred between the acid products and water when they pass through the column. Glycerol oxidation products also showed a change in the isotope distribution when the products were passed through the column. Thus, results from all

labeling experiments were obtained by direct infusion of the product solution in the mass spectrometer.

The initial TOFs [mol glycerol converted (mol Au_{surface})⁻¹ s⁻¹] for glycerol oxidation were calculated from initial global reaction rates. Selectivity is defined as moles of product formed divided by moles of C2 and C3 products formed. For ethanol oxidation, the TOF was based on the moles of acetic acid formed [mol acetic acid formed (mol Au_{surface})⁻¹ s⁻¹]. Although, acetic acid was the major reaction product, trace amounts of CO₂ were also observed.

Density functional theory (DFT) calculations were carried out using the Vienna ab initio simulation package (VASP) (S3-S5). The planewaves were constructed with an energy cutoff of 396 eV and Vanderbilt ultrasoft pseudopotentials (S3) with real space projection operators defining the features of the core region. The correlation and exchange energies were obtained using the Perdew-Wang 91 (PW91) generalized gradient approximation (GGA) functional (S6).

The binding energy (E_{be}) of each adsorbate was calculated as:

$$E_{be} = E_{surf+ads} - E_{surf} - E_{ads}$$

where:

$E_{surf+ads}$ \equiv energy of the surface + bound adsorbate

E_{surf} \equiv energy of the surface

E_{ads} \equiv energy of the adsorbate in vacuum

The vacuum cell calculations (E_{ads}) were performed spin-polarized using an 18x18x18 Å unit cell using the Γ -point version of VASP. A relaxation was performed until the maximum force upon each atom (maximum force, as it will be referred to) was less than 0.05 eV/Å; the forces were obtained using a fast Fourier transform (FFT) grid with a cutoff of twice the planewave cutoff; the wavefunctions were converged to within 10^{-6} eV. Because Pt and Au surfaces are non-magnetic, all calculations upon a surface were prepared non spin-polarized. A supercell lattice of 3x3 was chosen in order to accommodate the reacting species with minimal interaction between supercells. The Pt(111) and Au(111) surface were modeled with four metal layers and a vacuum size of 18 Å separating the periodic structure in the z -direction. The top two layers of the metal were allowed to relax while the lower two layers were fixed in their bulk lattice positions. For clarity, all surfaces shown in Figure 1 display only the top layer of the metal.

The structures were optimized in two steps. First, a rough relaxation was performed until the maximum force was less than 0.10 eV/Å; the forces were obtained using an FFT grid with a cutoff of 1.5x the planewave cutoff; the wavefunctions were converged to within 10^{-4} eV. Next, a relaxation was carried out until the max atom force was reduced beneath 0.05 eV/Å; the forces were obtained using an FFT grid with a cutoff of 2.5x the planewave cutoff; the wavefunctions were converged to within 10^{-6} eV. Both of these geometric optimizations were performed using a 3x3x1 k-point mesh with smearing of 0.20 eV. Finally, a 6x6x1 k-point mesh was used to determine the energy of the system. Here, the forces were obtained using an FFT grid with a cutoff of 1.5x the planewave cutoff. To test this three-step system, a sample of intermediates

were optimized using a 6x6x1 k-point mesh and an FFT grid size 2x the planewave cutoff to a force beneath 0.05 eV/Å. The results reveal a difference of binding energies less than 0.02 eV.

The activation barriers (E_{act}) were obtained as:

$$A + B \rightarrow TS \rightarrow C + D$$

$$E_{act} = E_{TS} + \delta E_{surf} - E_{surf+A} - E_{surf+B}$$

where:

$E_{surf+ads} \equiv$ energy of the surface + adsorbate (A or B)

$E_{surf} \equiv$ energy of the surface

$E_{TS} \equiv$ energy of the transition state

$\delta \equiv$ surface stoichiometric factor, for this example $\delta=1$

The structures of the transition states were determined using a combination of the nudged elastic band (NEB) (*S7-S9*) and dimer (*S10-14*) methods. The NEB approach was carried out using 16 images, a 3x3x1 k-point mesh and an FFT grid size 2x the planewave cutoff; the wavefunctions were converged to within 1×10^{-6} eV. The max atom force was converged to 0.20 – 0.50 eV/Å depending on the quality of the initial path and ability of the algorithms. The NEB calculations were performed only to provide an initial guess to the dimer algorithm, so forces lower than 0.50 eV/Å were not necessary.

The dimer algorithm was subsequently carried out using a 3x3x1 k-point mesh and an FFT grid size 2x the planewave cutoff; the wavefunctions were converged to within 1×10^{-6} eV. The distance between the dimer was set to 0.01 Å, the dimer was allowed to rotate four times or until the rotational force fell beneath 1 eV/Å. The max atom force was converged to 0.05 eV/Å.

As with the binding energy calculations, the energy of the transition state was then determined using a 6x6x1 k-point mesh with the same parameters specified in Step 3 of Table S4.

Supporting Text:

Glyceric acid as major product:

Semi-batch glycerol oxidation was studied over Au/C (WGC), Au/TiO₂ (WGC), Pt/C (Sigma-Aldrich), Pd/C (Sigma-Aldrich). The reaction was carried out with 0.3M glycerol and 0.6M NaOH dissolved in water at 333 K and 150 psig of O₂ pressure. Glyceric acid was found to be the major product (selectivity >60%) over all of the catalysts and a summary of the results can be found in Table 1. In addition to glyceric acid, glycolic and tartronic acid were also observed by the HPLC analysis. Trace amounts of oxalic, lactic and acetic acid were observed at high conversion of glycerol. In addition to these primary and secondary oxidation products, formic acid and Na₂CO₃ were also produced by the reaction. The C1 products (formic acid and Na₂CO₃) were formed in 1:1 or lower mole ratio to C2 products. The overall carbon balance for the glycerol oxidation typically closes to within 5%. Scheme S1 shows some possible reaction paths for glycerol oxidation over the supported Au catalysts.

Unlabeled glyceric acid (calcium glycerate) solution (0.05M) was used to obtain background spectra (Figure S2A) to compare with the results obtained during labeling experiments. Unlabeled glyceric acid solution in water gave only one significant peak at $m/z = 105$ in the electronegative ion mode (molecular weight of glyceric acid is 106).

Glycerol oxidation over Au/C, Au/TiO₂, Pt/C and Pd/C with ¹⁸O₂

Glycerol oxidation experiments were performed as described earlier. No labeled oxygen was observed in glyceric and tartronic (HOOCCHOHCOOH) acid products during glycerol oxidation over Au/C and Au/TiO₂ WGC with ¹⁸O₂. Figure 2 in the main text and Figure S2F show the mass spectra of glyceric acid and Figure S3D shows the mass spectrum for tartronic acid produced in these labeling experiments. The mass spectra in Figure S4C and S4E confirm incorporation of one ¹⁸O atom in the glycolic acid product (peak at mass 77), which could result from the proposed role of peroxide in C-C cleavage to give C2 (glycolic acid) product (S1). However, peaks at 75 and 77 in the mass spectrum of glycerol (reactant) solution (Figure S4G) overlap those of glycolic acid, thus complicating the interpretation. Figure S2B and S2C show the mass spectra of glyceric acid formed during glycerol oxidation with ¹⁸O₂ over Pt/C and Pd/C, respectively. Only one major peak ($m/z = 105$) corresponding to unlabeled glyceric acid (Figure S2A) was observed.

Glycerol oxidation over Au/C, Au/TiO₂, Pt/C and Pd/C in absence of added base

Table 1 shows the activity of all catalysts (Au/C, Au/TiO₂, Pt/C and Pd/C) in the absence of base for the semi-batch glycerol oxidation experiments. Gold showed no discernable activity for glycerol oxidation in the absence of base, however, glycerol was converted over both Pt and

Pd showed some activity with the former being much more active. Under neutral conditions, the highly reactive carbonyl group intermediates (viz. glyceraldehyde and dihydroxyacetone) were observed in significant amounts in the final product mixture. As described in the main text, glycerol oxidation was performed with $^{18}\text{O}_2$ over Pt/C in absence of base. In that case, no ^{18}O was observed in the glyceric acid product, as shown in Figure S2D.

Glycerol oxidation over Pt/C at various initial base concentrations

The effect of initial base concentration on the activity of glycerol oxidation over Pt/C catalyst was further studied by varying the initial NaOH concentration from 0 to 0.6M. The TOF for glycerol oxidation increased significantly with base concentration (See Table 1). Glycerol is a weak acid with the pKa of 14.15 (S14). Base facilitates the initial deprotonation of the alcohol during glycerol oxidation. The Henderson Hasselbalch (HH) equation was used to calculate the concentration of glycerolate (the deprotonated form of glycerol) in the reaction medium (S1).

$$\text{pH} = \text{pKa} + \log \left(\frac{[\text{glycerolate}]}{[\text{glycerol}]} \right)$$

The TOF increased linearly with the initial glycerolate concentration (Figure S1), which is consistent with earlier work in our lab that has shown analogous results over a gold catalyst (S1).

Test for oxygen exchange in glyceric, glycolic, tartronic and acetic acid with H_2^{18}O

Major glycerol and ethanol oxidation products (glyceric acid, glycolic acid, tartronic acid and acetic acid) were dissolved separately in labeled water (H_2^{18}O) and subjected to the reaction conditions without O_2 (0.6M NaOH, 333 K, 2 mg Au/C, 1 atm He) for the duration of typical

reaction time (3h). At the end of the reaction time, no significant incorporation of labeled oxygen was observed in the products, confirming that the glycerol and ethanol oxidation products are stable in water and do not exchange oxygen. The mass spectrum from these experiments can be found in S2E, S3B, S4B and S5B for glyceric, tartronic, glycolic and acetic acid, respectively.

Glycerol oxidation over Au/C and Au/TiO₂ with H₂¹⁸O solvent

Aqueous (H₂¹⁸O) phase glycerol (0.3M) oxidation was performed in presence of base (0.6M NaOH) and with ¹⁶O₂ as oxidizing agent over Au/C and Au/TiO₂ WGC catalyst at 333 K. The mass spectrum of product glyceric acid, shown in Figure 2 in the main text, illustrates the distribution of isotopomers ranging from the unlabeled (m/z = 105) to multiple labeled glyceric acid products (m/z = 107, 109, 111 and 113). Figure S3C and S4D show the mass spectra for tartronic and glycolic acid side products formed during this experiment. Incorporation of multiple ¹⁸O atoms into the side products was observed. Similar results were obtained in case of glycerol oxidation with H₂¹⁸O over the Au/TiO₂ catalyst (Figures S2G, S3E, S4F), indicating that O¹⁸ incorporation in the products was not affected by the composition of the support or the Au particle size.

Oxygen scrambling experiment with H₂¹⁸O for glyceraldehyde

During the base-catalyzed glyceraldehyde and dihydroxyacetone interconversion during glycerol oxidation (Scheme S1), exchange of oxygen atoms with water is believed to be prominent. Hence, a control experiment with glyceraldehyde (0.05M) in the presence of Au/C WGC and small amount of base (0.01M NaOH) was carried out in labeled H₂¹⁸O. Low concentration of base was used (0.01M as compared to 0.6M under reaction conditions) to avoid

degradation of glyceraldehyde. Mass spectrometry confirmed that ^{18}O was incorporated into dihydroxyacetone (DHA) within 5 minutes (Figure S6).

Ethanol oxidation over Au/C and Au/TiO₂ with $^{18}\text{O}_2$

Ethanol oxidation experiments were performed as described earlier. No ^{18}O was observed in the acetic acid product during ethanol oxidation over Au/C WGC with $^{18}\text{O}_2$. Figure S5C shows the mass spectrum of the acetic acid product. Figure S5E shows the mass spectrum for acetic acid formed during ethanol oxidation over Au/TiO₂ with $^{18}\text{O}_2$. Again, only one peak ($m/z = 59$) corresponding to unlabeled acetic acid (Figure S5A) was observed.

Ethanol oxidation over Au/C, Au/TiO₂ and Pt/C in absence of added base.

Table S1 summarizes the reaction rate results from all of the catalysts (Au/C, Au/TiO₂, Pt/C) in absence of base for ethanol oxidation experiments in the semi-batch reactor. As in the case of glycerol oxidation, no discernable activity was observed in absence of base for ethanol oxidation over Au catalysts, however, some activity was observed over a Pt catalyst. Under neutral conditions, the highly reactive carbonyl group intermediate (acetaldehyde) was also observed in the final product mixture over the Pt catalyst.

Ethanol oxidation over Au/C and Au/TiO₂ with H₂ ^{18}O solvent

Aqueous (H₂ ^{18}O) phase ethanol (0.3M) oxidation was performed in the presence of base (0.6M NaOH) and with $^{16}\text{O}_2$ over Au/C and Au/TiO₂ (WGC) catalysts at 333 K. The mass spectra for acetic acid are shown in Figure S5D and S5F. Two ^{18}O atoms were observed in the product acetic acid. These results, along with those from glycerol oxidation indicate that neither

the support composition nor the Au particle size affect the overall reaction path for alcohol oxidation in liquid water.

The effect of solution molecules on the reaction energetics and barriers

The solution/metal interface was modeled by optimizing 24 water molecules within the vacuum region of the 3x3 unit cell thus providing a density of water at the surface of 0.86 g/cm³. The optimized structure is consistent with the hexagonally closed packed ice-like structure (*S15*, *S16*) at the metal interface and is comprised of four repeating layers as shown in Figure S8. In the layer closest to the surface, three water molecules are bound atop on the metals in the hexagonal arrangement. During the calculation of binding energies and activation barriers, a bound water is removed to create a vacancy on the surface; through optimization the waters surrounding the adsorbates are free to expand due to repulsive interactions or to rearrange thus maximizing hydrogen bonding opportunities. For some reactions involving hydroxide or a water molecule, the hydroxide or water originates from the surrounding solvent network.

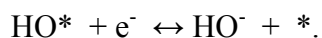
The effect of the explicit water molecules, which make up the solution phase, on reaction barriers studied depends upon the interactions between the reactant and transition state with the surrounding water molecules. In many cases, the effect of solvation is similar between the two states, resulting in only small changes in the activation barriers as shown in Table S3. For dehydrogenation reactions such as 1a, 2a and 4a, there is very little difference between the hydrogen bonding abilities of the reactant and transition state, and the surrounding water only crowds the catalyst surface resulting in a slightly increased barrier. Water plays a much more significant role, however, when there is a change in the dipole orientation between the reactant

and the transition state, as this can lead to a change in the number of hydrogen bonds or a change in the polarizability, both of which can stabilize one state over the other. This can be seen for example in reaction 5 where the barriers for OH dissociation increase on both Au(111) and Pt(111) in the presence of water as the water more effectively stabilizes the OH* reactant over the O*-like transition state as a result of more hydrogen bonds. Similarly, the decrease in hydrogen bonding that results in moving from OH* to H₂O* in reaction 6 also acts to increase the activation barrier. Among the kinetically significant reactions involved in the oxygen reduction reaction with water, reaction 8b demonstrates a significant decrease in activation barrier in liquid water, which is expected due to the creation of hydrogen bonding species.

Overall, the addition of waters of solvation has a relatively minor influence on the alcohol oxidation sequence because the important role of hydroxide as a hydrogen acceptor was preserved. However, the waters of solvation shift the barriers of the reactions involved in the oxygen reduction sequence to favor the production of hydrogen peroxide.

Adsorption of hydroxide on Au surfaces

Despite the strong solvation energy (-1.3 eV) of hydroxide, there is an equilibrium between OH⁻ in solution and that which is on the surface as the binding energies of OH* on water-covered Pt (111) and Au(111) surfaces are also sufficiently strong at -2.4 and -2.1 eV. Furthermore, the mobility of OH⁻ in the aqueous phase is enhanced through the rapid exchange of protons between water and OH⁻ as the barrier for proton transfer is only 10 kJ mol⁻¹, which establishes an equilibrium between OH(aq) and OH* described by:



In addition to this equilibrium, the oxygen reduction reaction which occurs on both Pt and Au surfaces in alkaline media, even at low electrochemical potentials, readily forms OH ions on the surface. Furthermore, experimental evidence strongly supports the presence of hydroxide on single crystal Pt and Au surfaces that form as a result of O₂ reduction as well as through the competitive adsorption of electrolyte anions present in both acidic as well as alkaline media. While Pt is the most active metal for the oxygen reduction reaction in acidic media, Au, or more specifically Au(100), demonstrates the highest activities in basic media as it allows for appreciable OH coverage but prevents poisoning of the surface. The competitive adsorption of hydroxide on Au(100) is strong enough to lift the hex to 111 surface reconstruction (*S17*) and is thought to be critical in catalyzing O₂ reduction on this surface (*S18, S19*).

Gerwirth et al. demonstrated appreciable coverages of hydroxide intermediates on Au through the use of in-situ surface enhanced Raman scattering spectroscopy over a range of different potentials (*S20-S22*). Hydroxide is present even at lower potentials on Au. Lastly, it is well established that OH/H₂O interfaces will form as a result of the reaction of oxygen and water on both Pt and Au(111) surfaces even under UHV conditions (*S16, S23*).

Supporting Figures:

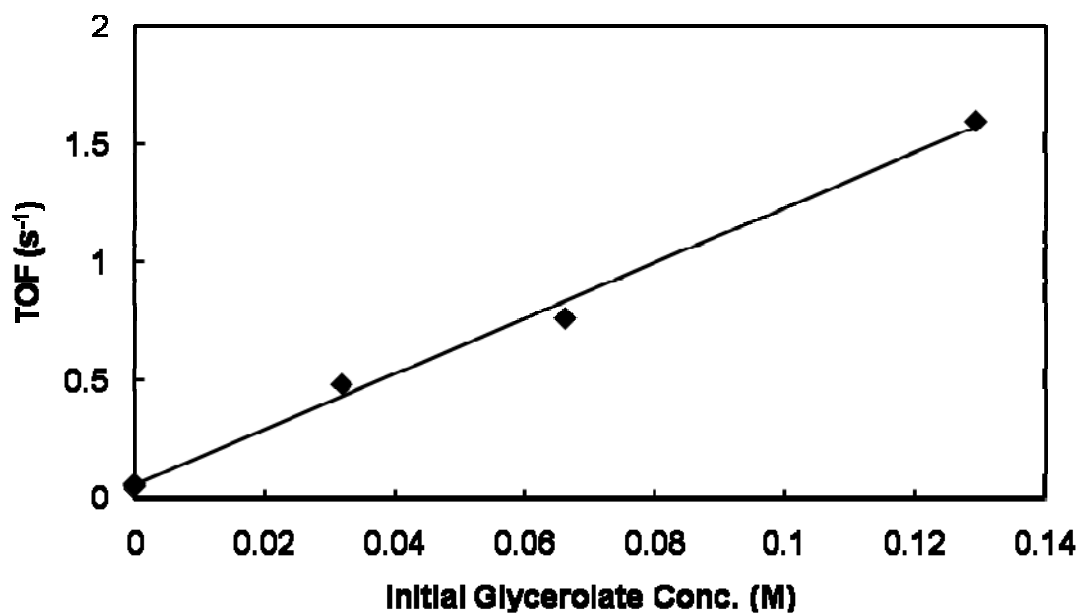


Figure S1: Turnover frequency for glycerol oxidation over Pt/C at various initial base concentrations. See the footnotes of Table 1 for the reaction conditions. The initial glycerolate concentration was determined from the Henderson Hasselbalch (HH) equation.

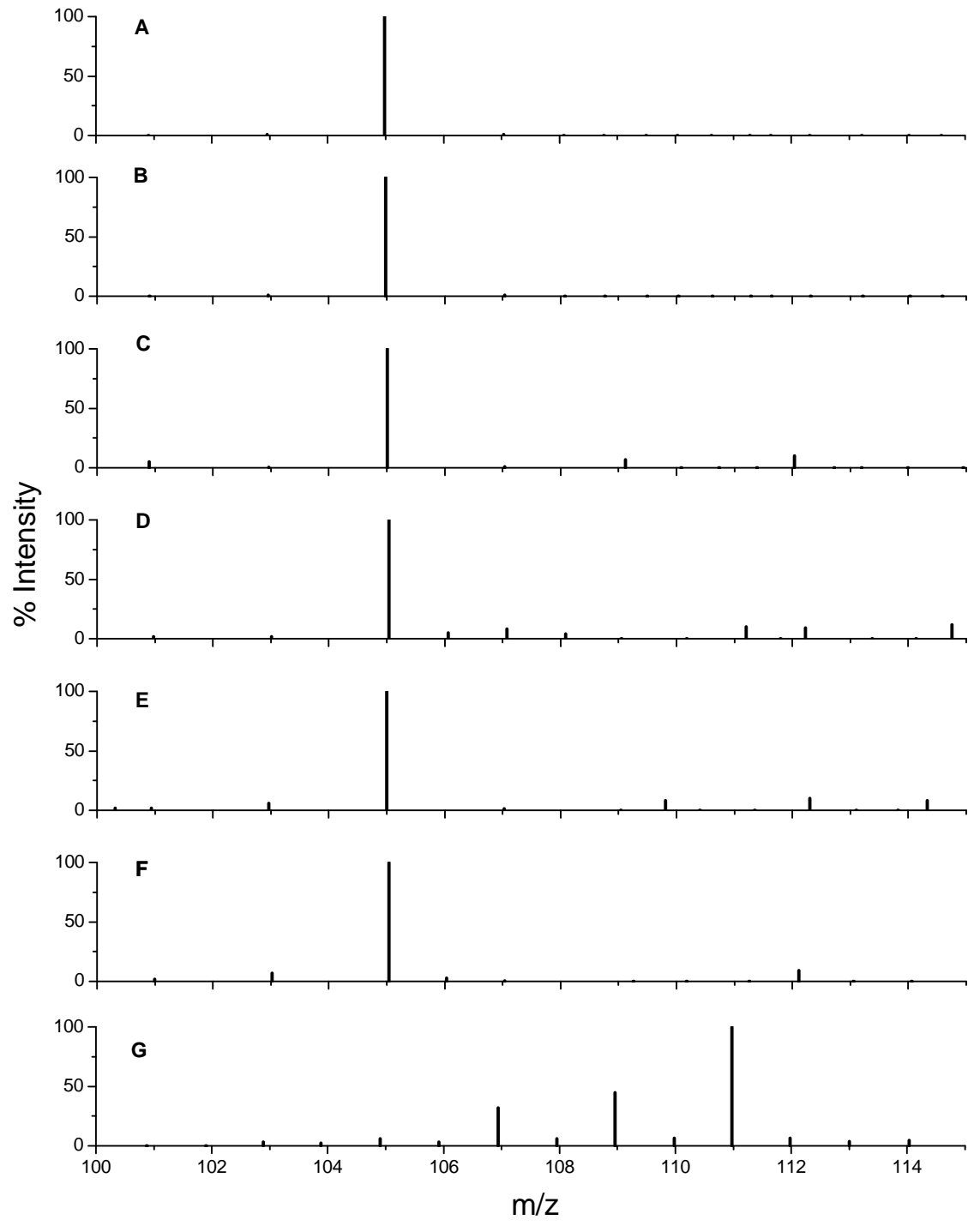


Figure S2. Mass spectra (electronegative ion mode) of glyceric acid (M.W. 106) in (A) its unlabeled solution (0.05M calcium glycerate in water), (B) glycerol oxidation over Pt/C with $^{18}\text{O}_2$ and H_2^{16}O , (C) glycerol oxidation over Pd/C with $^{18}\text{O}_2$ and H_2^{16}O , (D) glycerol oxidation over Pt/C with $^{18}\text{O}_2$ and H_2^{16}O in absence of added base, (E) glyceric acid in H_2^{18}O with added base and Au/C catalyst, (F) glycerol oxidation over Au/TiO₂ with $^{18}\text{O}_2$ and H_2^{16}O , (G) glycerol oxidation over Au/TiO₂ with $^{16}\text{O}_2$ and H_2^{18}O . Common reaction conditions: 0.6 M NaOH, 333K, unless stated otherwise.

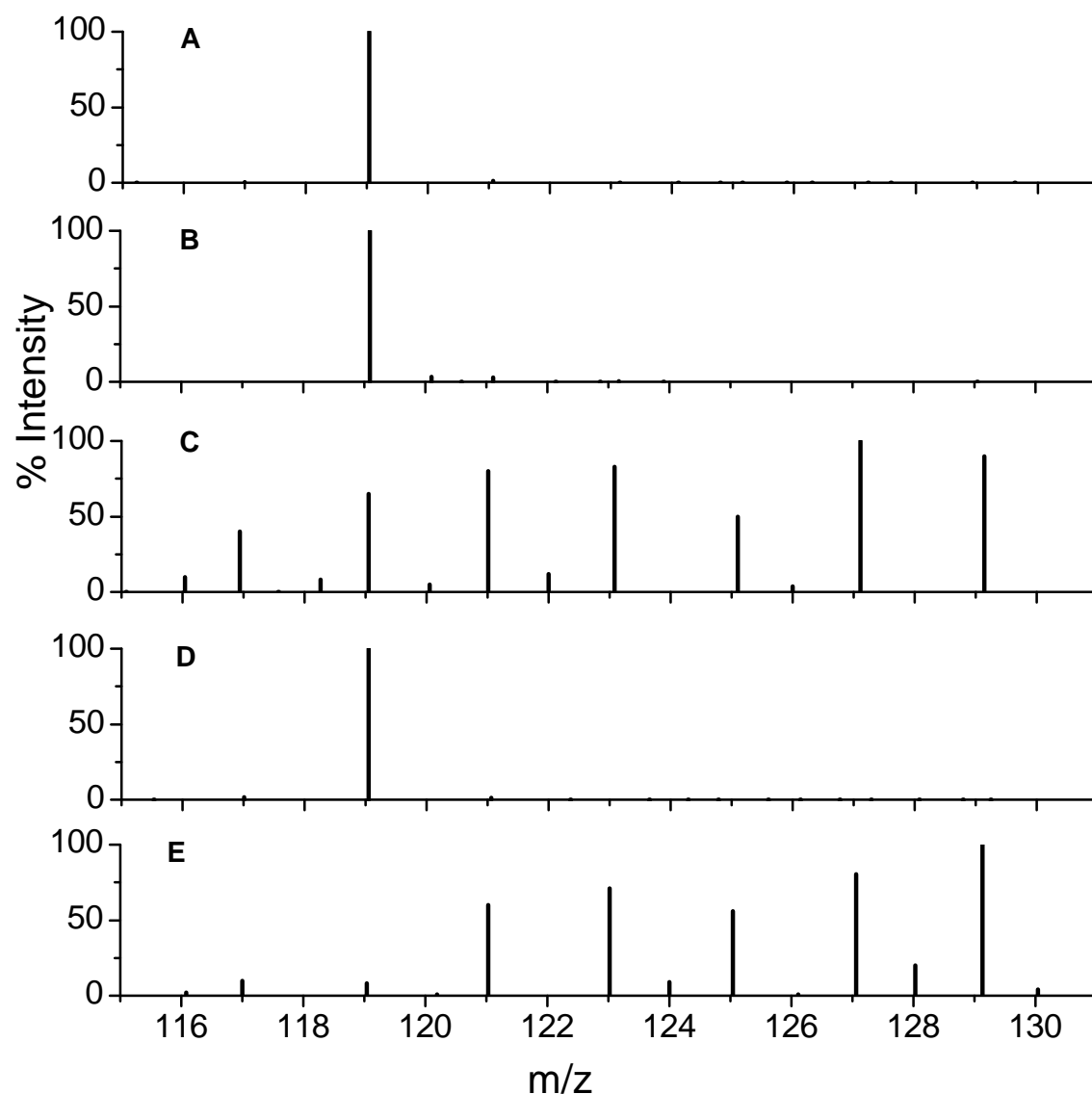


Figure S3. Mass spectra (electronegative ion mode) of tartronic acid (M.W. 120) in (A) its unlabeled solution (0.05M), (B) tartronic acid in H_2^{18}O with added base and Au/C catalyst, (C) glycerol oxidation over Au/C WGC with $^{16}\text{O}_2$ and H_2^{18}O , (D) glycerol oxidation over Au/TiO₂ WGC with $^{18}\text{O}_2$ and H_2^{16}O , (E) glycerol oxidation over Au/TiO₂ WGC with $^{16}\text{O}_2$ and H_2^{18}O . Common reaction conditions: 0.6 M NaOH, 333K.

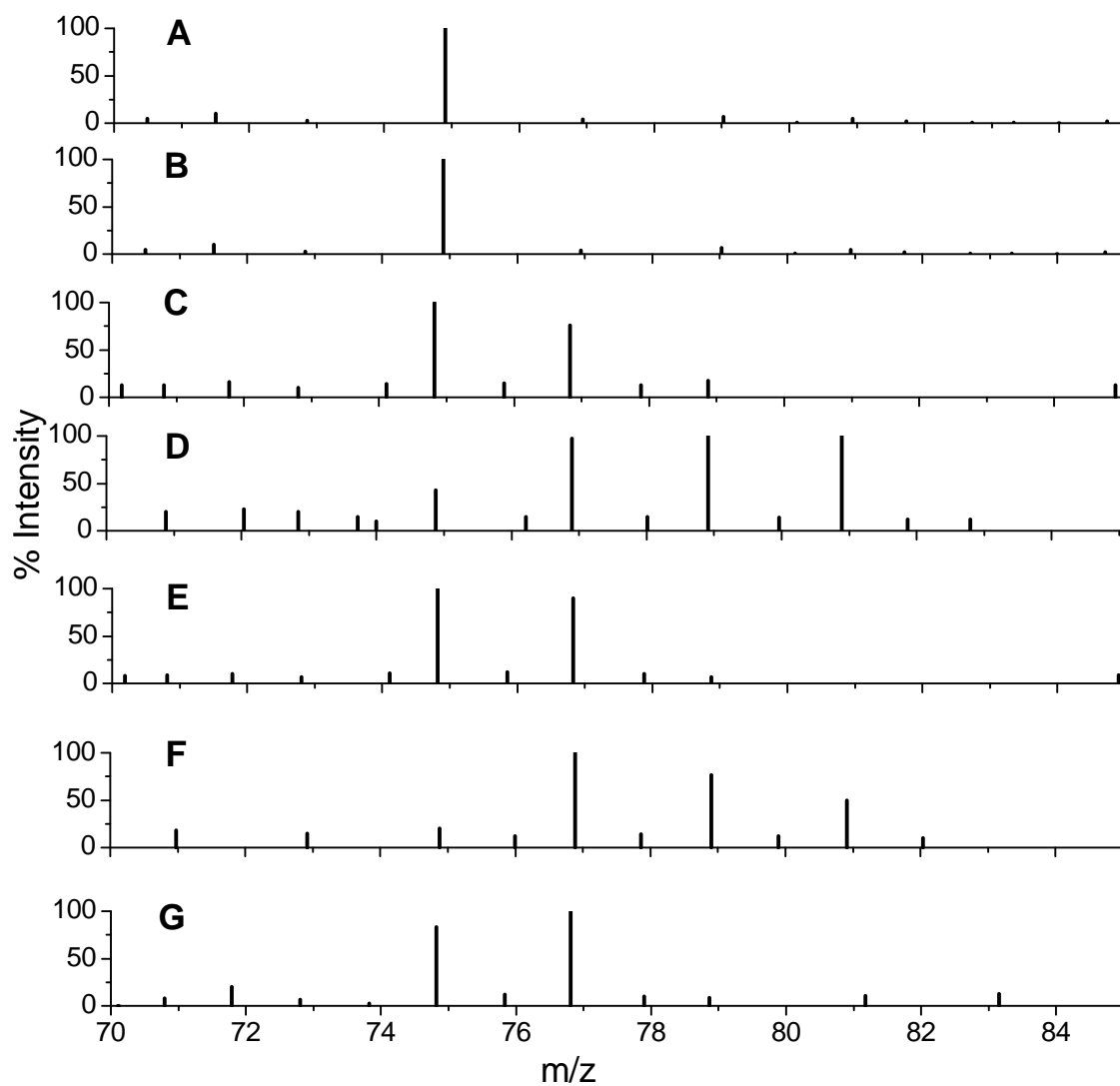


Figure S4. Mass spectra (electronegative ion mode) of glycolic acid (M.W. 76) in (A) its unlabeled solution (0.05M), (B) glycolic acid in H_2^{18}O with added base and Au/C catalyst, (C) glycerol oxidation over Au/C WGC with $^{18}\text{O}_2$ and H_2^{16}O , (D) glycerol oxidation over Au/C WGC with $^{16}\text{O}_2$ and H_2^{18}O , (E) glycerol oxidation over Au/TiO₂ WGC with $^{18}\text{O}_2$ and H_2^{16}O , (F) glycerol oxidation over Au/TiO₂ WGC with $^{16}\text{O}_2$ and

H_2^{18}O , (G) Fragmentation peaks observed in mass spectrum of glycerol (reactant) solution. Common reaction conditions: 0.6 M NaOH, 333K.

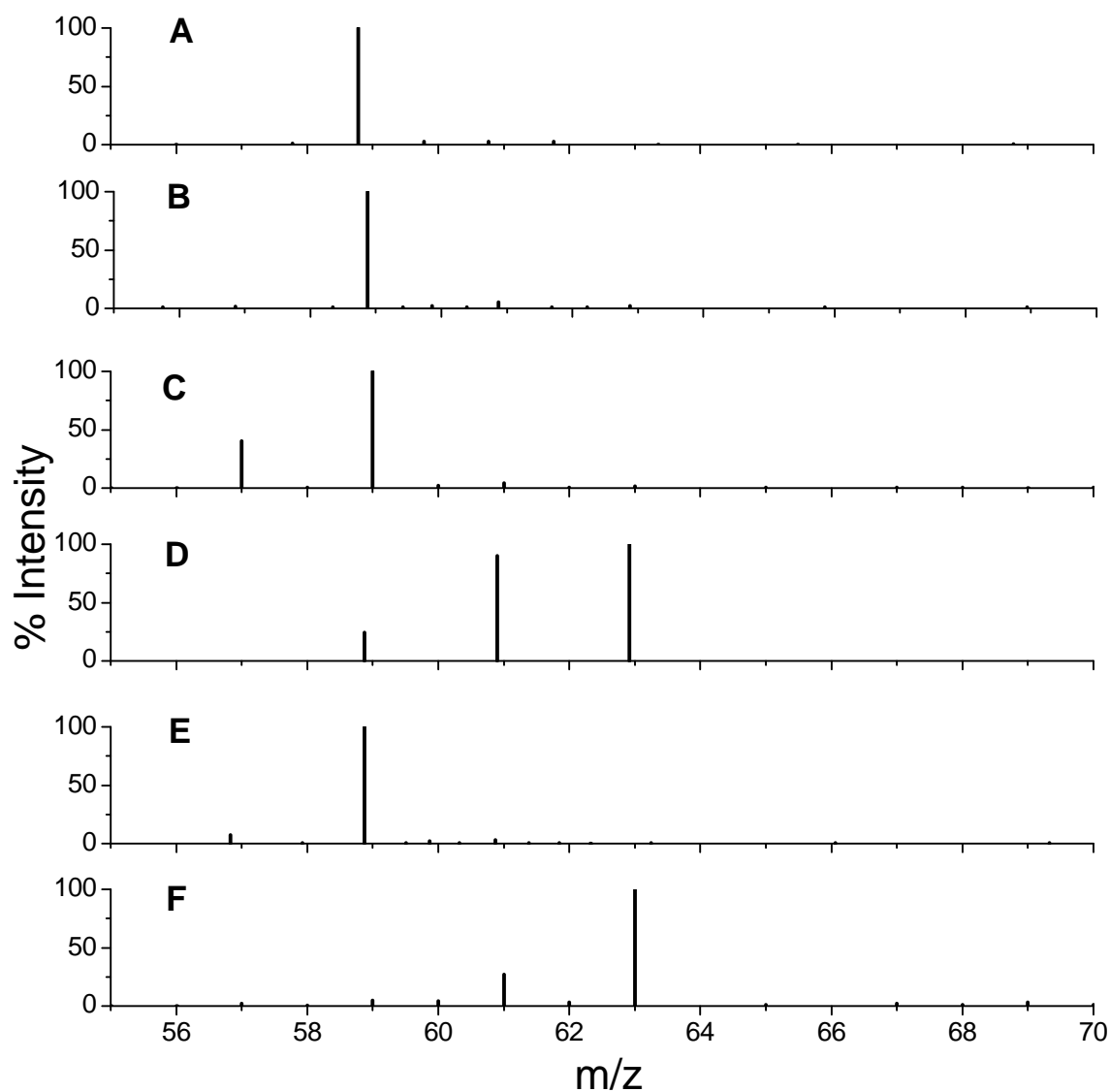


Figure S5. Mass spectra (electronegative ion mode) of acetic acid (M.W. 60) in (A) its unlabeled solution (0.05M), (B) acetic acid in H₂¹⁸O with added base and Au/C catalyst, (C) ethanol oxidation over Au/C WGC with ¹⁸O₂ and H₂¹⁶O, (D) ethanol oxidation over Au/C WGC with ¹⁶O₂ and H₂¹⁸O, (E) ethanol oxidation over Au/TiO₂ WGC with ¹⁸O₂ and H₂¹⁶O, (F) ethanol oxidation over Au/TiO₂ WGC with ¹⁶O₂ and H₂¹⁸O. Common reaction conditions: 0.6 M NaOH, 333K.

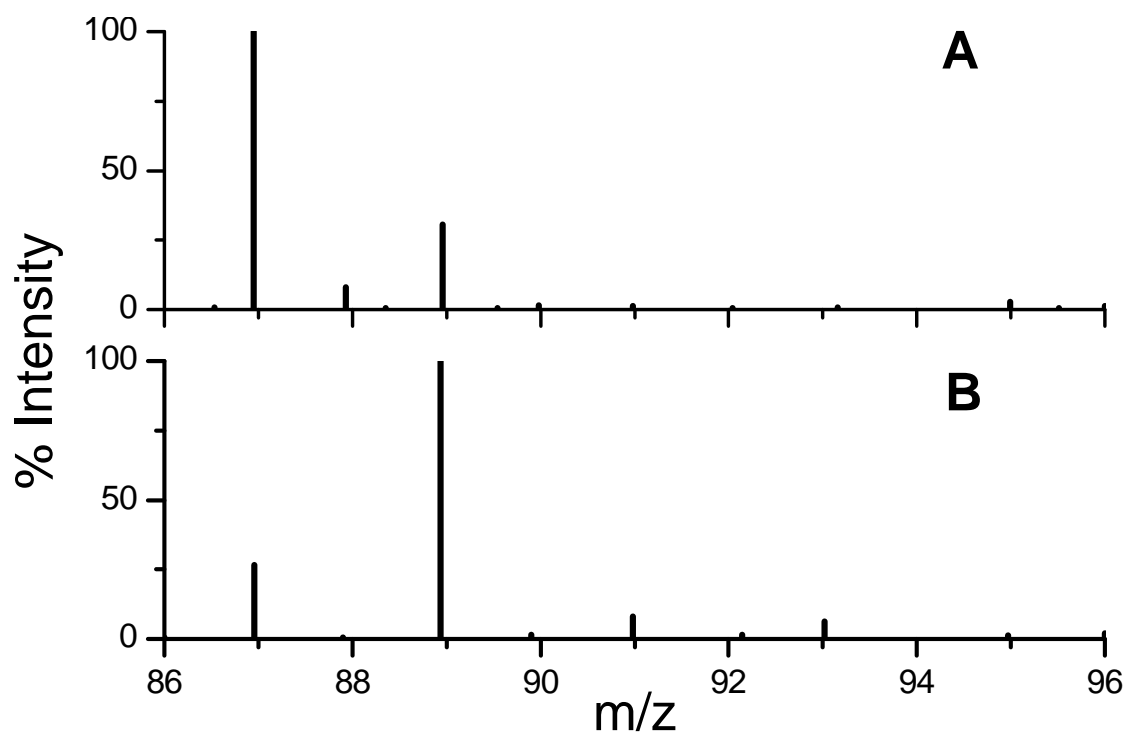


Figure S6. LC Mass spectra (electronegative ion mode) of dihydroxyacetone (M.W. 90) product from HPLC separation in (A) its unlabeled solution (0.05M), (B) oxygen exchange experiment of glyceraldehyde (0.05M) in H_2^{18}O and in presence of added base (0.01M) and Au/C. The ratios of isotopomers can not be quantitatively determined because of partial exchange with the HPLC column. HPLC column was used only for this experiment to allow for separation between glyceraldehyde (M.W. 90) and dihydroxyacetone (M.W. 90).

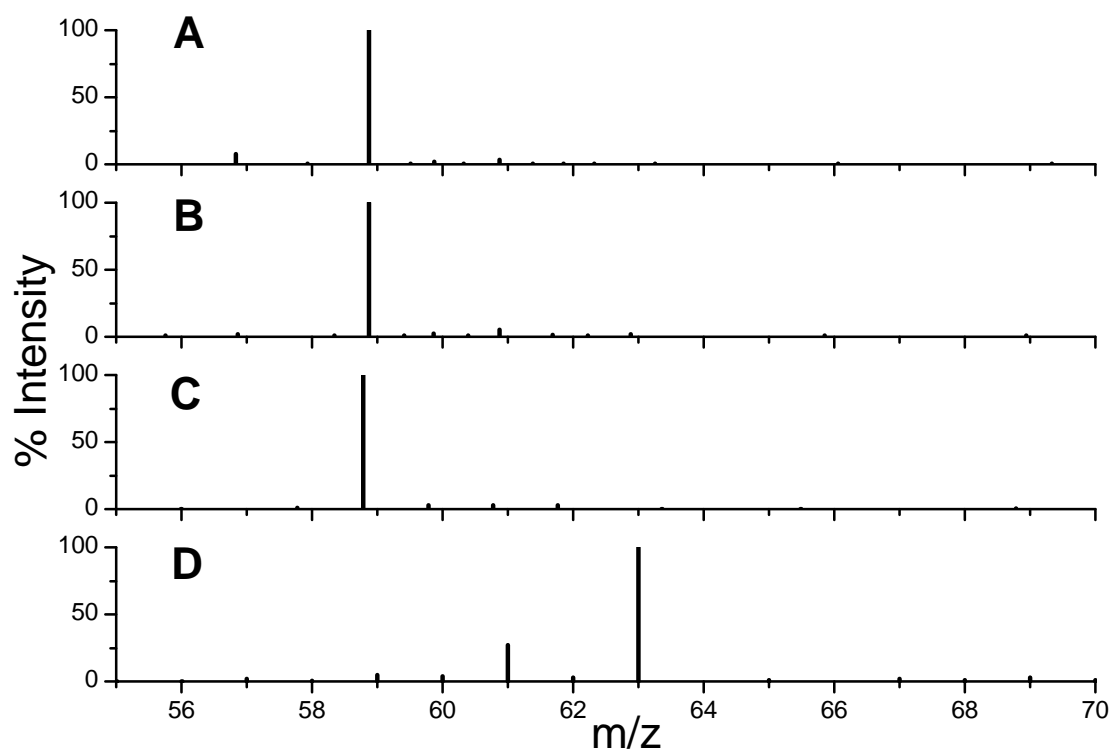


Figure S7. Mass spectra (electronegative ion mode) of acetic acid (M.W. 60) formed during ethanol oxidation over Au/TiO₂ with ¹⁸O₂ and H₂¹⁶O analyzed by (A) liquid chromatograph (HPLC) followed by MS detection and (B) direct infusion in MS; and formed during ethanol oxidation over Au/TiO₂ with ¹⁶O₂ and H₂¹⁸O analyzed by (C) liquid chromatograph (HPLC) followed by MS detection and (D) direct infusion in MS. Common reaction conditions: 0.6 M NaOH, 333K.

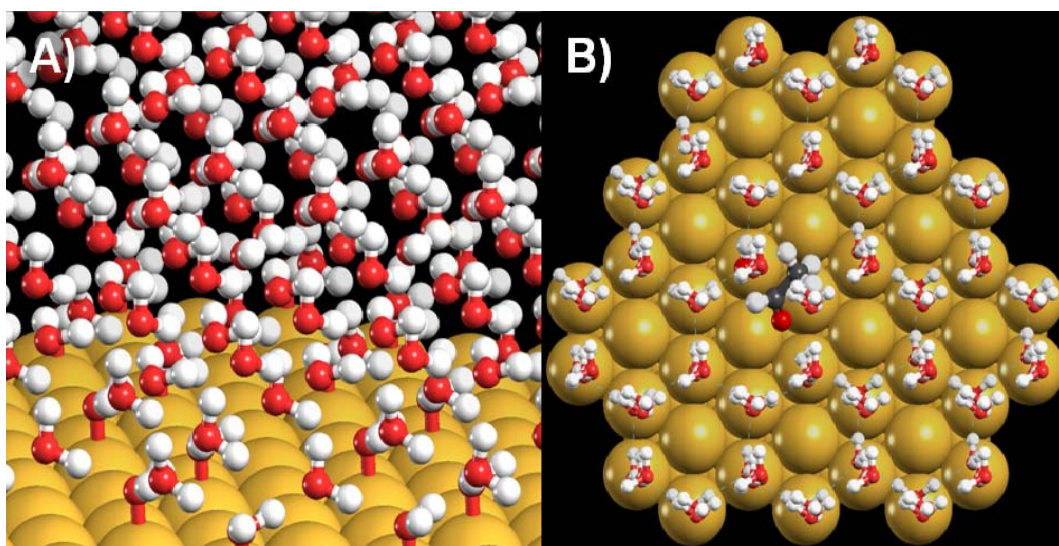
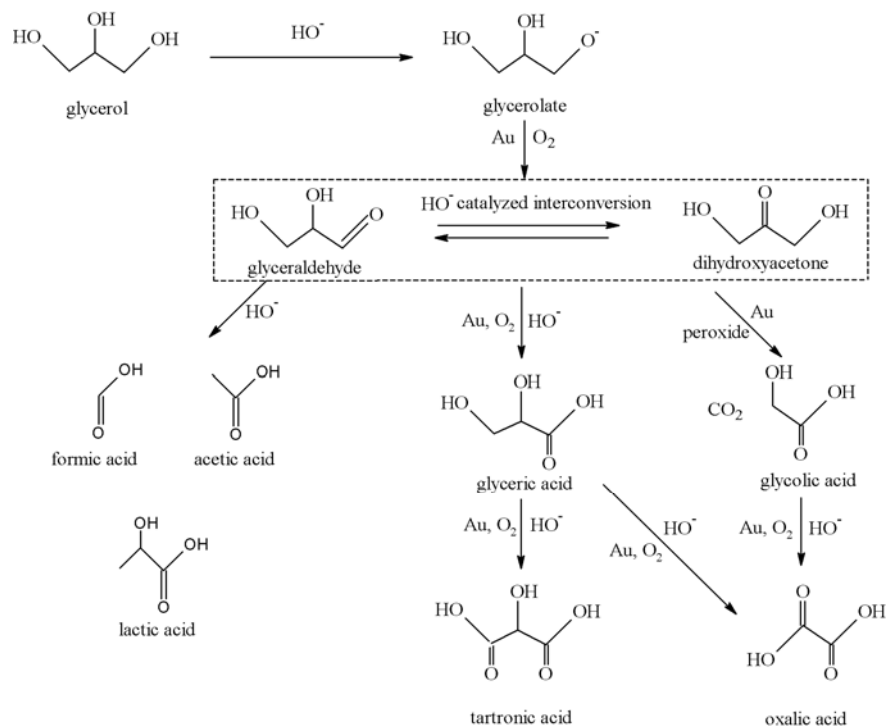


Figure S8. Water bi-layer on a metal surface. A) Side view of the aqueous/metal interface model made up of multi bi-layers with 24 water molecules per unit cell (expanded here in the x and y direction to cover 3 unit cells) shown on Au(111). B) Top view of a transition state from acetaldehyde to ethoxy-diol over Au(111). This view highlights the hexagonal, ice-like structure of the solution.

Supporting Schemes:



Scheme S1: Possible Reaction Paths for Glycerol Oxidation over Supported Au Catalysts
(Adapted from Ketchie *et al.*, *Top. Catal.* **44**, 307 (2007)).

Supporting Tables:

Table S1: Ethanol Oxidation over Au/C, Au/TiO₂ and Pt/C in Liquid Water

Catalyst	NaOH: ethanol (mol:mol)	TOF (s ⁻¹)	% Selectivity*	
			Acetic Acid	Acetaldehyde
Au/C	2.0	0.30	100	0.0
Au/TiO ₂	2.0	0.46	100	0.0
Pt/C	2.0	0.04	100	0.0
Au/C ^a	0.0	0.0	-	-
Au/TiO ₂ ^a	0.0	0.0	-	-
Pt/C ^a	0.0	0.01	67	33

Reaction conditions: 0.3M ethanol (E), 5mL, 333 K, pO₂ 150 psig, E: Au = E: Pt = 5000 (mol:mol), t = 2h; ^a t = 5h; Dispersion: Au/C = 0.05, Au/TiO₂ = 0.29, Pt/C = 0.43. * The trace amount of CO₂ observed is not included in selectivity calculations.

Table S2: Characteristic Properties of the Au/C, Au/TiO₂, Pt/C and Pd/C Catalysts

Catalyst	Metal Weight %	Avg. Metal Particle Diameter (nm)	Surface Avg. Diameter (nm)	Dispersion*
Au/C	0.8	10.5 ^a	18.8 ^b	0.05 ^c
Au/TiO ₂	1.6	3.5 ^a	-	0.29 ^d
Pt/C	1.0	-	-	0.43
Pd/C	2.9	-	-	0.33

* Dispersion were calculated by H₂ chemisorption for Pt/C and Pd/C and was based on Au particle size for the Au catalysts.

^a from TEM analysis – provided by World Gold Council.

^b surface average diameter ($\Sigma d^3 / \Sigma d^2$) (I).

^c inverse of surface average diameter.

^d inverse of average metal particle diameter.

Table S3: Selected reaction energies (kJ mol^{-1}) and activation barriers (kJ mol^{-1}) for the oxidation of ethanol to acetic acid over Au(111) and Pt(111).

	Reaction	Au (111)				Pt (111)			
		w/o Solvent		w/ Solvent		w/o Solvent		w/ Solvent	
		ΔH_{RXN}	E_{ACT}						
1a	$\text{CH}_3\text{CH}_2\text{OH}^* + * \rightarrow \text{CH}_3\text{CH}_2\text{O}^* + \text{H}^*$	164	189	196	204	84	92	98	116
1b	$\text{CH}_3\text{CH}_2\text{OH}^* + \text{OH}^* \rightarrow \text{CH}_3\text{CH}_2\text{O}^* + \text{H}_2\text{O}^*$	-13	12	13	22	7	25	-5	18
2a	$\text{CH}_3\text{CH}_2\text{O}^* + * \rightarrow \text{CH}_3\text{CHO}^* + \text{H}^*$	-26	45	-40	46	-54	4	-62	15
2b	$\text{CH}_3\text{CH}_2\text{O}^* + \text{OH}^* \rightarrow \text{CH}_3\text{CHO}^* + \text{H}_2\text{O}^*$	-203	15	-222	12	-131	11	-165	24
3	$\text{CH}_3\text{CHO}^* + \text{OH}^* \rightarrow \text{CH}_3\text{CH}(\text{OH})\text{O}^* + *$	-42	17	-33	5	-44	15	-5	5
4a	$\text{CH}_3\text{CH}(\text{OH})\text{O}^* + * \rightarrow \text{CH}_3\text{COOH}^* + \text{H}^*$	-80	8	-151	21	-85	8	-154	13
4b	$\text{CH}_3\text{CH}(\text{OH})\text{O}^* + \text{OH}^* \rightarrow \text{CH}_3\text{COOH}^* + \text{H}_2\text{O}^*$	-257	22	-334	29	-161	20	-258	17
5	$\text{OH}^* + * \rightarrow \text{O}^* + \text{H}^*$	158	202	176	222	16	106	49	126
6	$\text{OH}^* + \text{H}^* \rightarrow \text{H}_2\text{O}^* + *$	-173	17	-183	39	-75	22	-103	30
7	$\text{O}_2^* + * \rightarrow \text{O}^* + \text{O}^*$	3	126	41	105	-133	67	-129	64
8a	$\text{O}_2^* + \text{H}^* \rightarrow \text{OOH}^* + *$	-121	13	-161	25	-16	43	-47	57
8b	$\text{O}_2^* + \text{H}_2\text{O}^* \rightarrow \text{OOH}^* + \text{OH}^*$	38	43	-4	16	49	54	16	18
9	$\text{OOH}^* + * \rightarrow \text{OH}^* + \text{O}^*$	-33	57	-56	83	-133	26	-131	52
10a	$\text{OOH}^* + \text{H}^* \rightarrow \text{HOOH}^* + *$	-145	11	-146	19	-20	40	-49	46
10b	$\text{OOH}^* + \text{H}_2\text{O}^* \rightarrow \text{HOOH}^* + \text{OH}^*$	60	65	37	48	5	37	-101	41
11	$\text{HOOH}^* + * \rightarrow \text{OH}^* + \text{OH}^*$	-45	46	-86	71	-128	17	-131	29

Table S4: Three-step scheme for surface DFT calculations.

	Step 1	Step 2	Step 3
wavefunction convergence	1×10^{-4}	1×10^{-6}	1×10^{-3}
FFT grid size	1.5x	2x	1.5x
maximum force	0.10	0.05	--
k-point mesh	3x3x1	3x3x1	6x6x1

Supporting References:

- S1. W. C. Ketchie, M. Murayama, R. J. Davis, Promotional effect of hydroxyl on the aqueous phase oxidation of carbon monoxide and glycerol over supported Au catalysts. *Top. Catal.* **44**, 307 (2007).
- S2. W. C. Ketchie, M. Murayama, R. J. Davis, Selective oxidation of glycerol over carbon-supported AuPd catalysts. *J. Catal.* **250**, 264 (2007).
- S3. G. Kresse, J. Furthmueller, Efficient iterative schemes for ab initio total-energy calculations using a plane-wave basis set. *Phys. Rev. B* **54**, 11169-11186 (1996).
- S4. M. Methfessel, A. T. Paxton, High-precision sampling for Brillouin-zone integration in metals. *Phys. Rev. B* **40**, 3616-3621 (1989).
- S5. P. E. Blochl, O. Jepsen, O. K. Andersen, Improved tetrahedron method for Brillouin-zone integrations. *Phys. Rev. B* **49**, 16223-16233 (1994).

- S6. J. P. Perdew *et al.*, Atoms, molecules, solids, and surfaces: applications of the generalized gradient approximation for exchange and correlation. *Phys. Rev. B* **46**, 6671-6687 (1992).
- S7. G. Henkelman, H. Jónsson, Improved tangent estimate in the nudged elastic band method for finding minimum energy paths and saddle points. *J. Chem. Phys.* **113**, 9978 (2000).
- S8. G. Henkelman, B. P. Uberuaga, H. Jónsson, A climbing image nudged elastic band method for finding saddle points and minimum energy paths. *J. Chem. Phys.* **113**, 9901 (2000).
- S9. D. Sheppard, R. Terrell, G. Henkelman, Optimization methods for finding minimum energy paths. *J. Chem. Phys.* **128**, 134106 (2008).
- S10. G. Henkelman, H. Jónsson, A dimer method for finding saddle points on high dimensional potential surfaces using only first derivatives. *J. Chem. Phys.* **111**, 7010 (1999).
- S11. R. A. Olsen, G. J. Kroes, G. Henkelman, A. Arnaldsson, H. Jónsson, Comparison of methods for finding saddle points without knowledge of the final states. *J. Chem. Phys.* **121**, 9776 (2004).
- S12. A. Heyden, A. T. Bell, F. J. Keil, Efficient methods for finding transition states in chemical reactions: comparison of improved dimer method and partitioned rational function optimization method. *J. Chem. Phys.* **123**, 224101 (2005).
- S13. J. Kästner and P. Sherwood, Superlinearly converging dimer method for transition state search. *J. Chem. Phys.* **128**, 014106, (2008).
- S14. D. Lide, *CRC Handbook of Chemistry and Physics* **71** (2006).

- S15. D. Doering and T. Madey, The adsorption of water on clean and oxygen-dosed ruthenium(001). *Surf. Sci.* **123**, 305 (1982).
- S16. M. Henderson, The interaction of water with solid surfaces: fundamental aspects revisited. *Surf. Sci. Reports.* **46**, 1 (2002).
- S17. B.B. Blizanac, C.A. Lucas, M.E. Gallagher, M. Arenz, P.N. Ross, and N.M. Markovic, Anion adsorption, CO oxidation, and oxygen reduction reaction on a Au(100) surface: The pH effect. *J. Phys. Chem. B.* **108**, 625 (2004).
- S18. R.R. Adzic, A.V. Tripkovic, and N.M. Markovic, Structural effects in electrocatalysis: Oxidation of formic acid and oxygen reduction on single-crystal electrodes and the effects of foreign metal adatoms. *J. Electroanal. Chem.* **150**, 79 (1983).
- S19. N.M. Markovic, R.R. Adzic, and V.B. Vesovic, Structural effects in electrocatalysis - oxygen reduction on the gold single-crystal electrodes with (110) and (111) orientations. *J. Electroanal. Chem.* **165**, 121 (1984).
- S20. J. Kim and A.A. Gewirth, Mechanism of oxygen electroreduction on gold surfaces in basic media *J. Phys. Chem. B.* **110**, 2565 (2006).
- S21. X. Li and A.A. Gewirth, SERS study of hydrogen peroxide electroreduction on a Pb-modified Au electrode. *J. Raman Spectroscopy.* **36**, 715 (2005).
- S22. A.A. Gewirth and M.S. Thorum, Electroreduction of dioxygen for fuel-cell applications: materials and challenges. *Inorg. Chem.* **49**, 3557 (2010).
- S23. A. Shavorskiy, M.J. Gladys, and G. Held, Chemical composition and reactivity of water on hexagonal Pt-group metal surfaces. *Phys. Chem. Chem. Phys.* **10**, 6150 (2008).